SI Appendix

Fuel and Oxygen Harvesting from Martian Regolithic Brine

Pralay Gayen[#], *Shrihari Sankarasubramanian*[#], *Vijay K. Ramani*[*]

Center for Solar Energy and Energy Storage and Department of Energy, Environmental and Chemical Engineering, Washington University in St. Louis, MO 63130, USA

[#]Equal contribution

[*]Corresponding author at: Department of Energy, Environmental and Chemical Engineering, Washington University in St. Louis, MO 63130, USA

E-mail address: ramani@wustl.edu (Vijay Ramani)

Phone No.: +13149357924

This PDF file includes:

Materials and Methods

Results and Discussions

Figures S1 to S17

Table S1 and S2

References

S1. Evidence of terrestrial and subsurface water on Mars

From May 25, 2008 to August, 2008 NASA's Phoenix lander explored the polar regions of Mars to understand 1) polar climate and weather, 2) atmospheric composition with an emphasis on water vapor, ice, dust and CO_2 (see comparison with Earth's atmosphere in **Figure S1**), 3) role of water in shaping Martian geography, 4) aqueous chemistry, organic content and confirmation of subsurface ice and 5) history of water and its effect on the possible presence of life on Mars. The lander carried a thermal and evolved gas analyzer (TEGA) to analyze vaporized regolith for water vapor, CO_2, minerals and traces of water ice (1). Supplementing the TEGA, the lander also carried a microscopy, electrochemistry, and conductivity analyzer (MECA) incorporating a wet chemistry lab (WCL) with thermal and electrical conductivity probes to measure the chemical composition of Martian soil, thermal and electrical conductivity (2). TEGA's mass spectrometer detected water vapor at 0 ^{o}C while the slightly alkaline soil (pH = 7.7) and bound water with moderate salinity was detected by WCL and confirmed by TEGA (3). A significant discovery was the detection of perchlorate salts in the soil at concentrations as high as 0.5 wt% (**Table S1**). The high concentrations of oxidative perchlorate may limit lifeforms to highly adapted extremophiles (4). Nevertheless, the perchlorates also enable the presence of liquid water even at the average Martian terrestrial temperature of -63 ^{o}C due to its ability to depress the freezing point of water below -60 ^{o}C (5)(6). Recently published data obtained by the Mars Advanced Radar for Subsurface and Ionosphere Sounding (MARSIS) instrument on-board the Mars Express spacecraft shows that multiple sub-glacial water bodies presently exist underneath the Martian south pole deposits at Ultimi Scopuli (7).

S2. Oxygen production routes on Mars

NASA is aiming to produce oxygen on Mars to serve as a oxidizer for a sample return mission and to provide life support for astronauts during a possible 2030 landing mission (8). NASA and MIT have developed the MOXIE (Mars OXygen In situ resource utilization Experiment) for oxygen production from the abundant CO_2 (96 %) in the Martian atmosphere via solid oxide electrolysis for the Mars 2020 mission (9). MOXIE will produce CO and O_2 and separate the gases as breathable O_2 needs to be highly pure (> 99.6 %) and completely separated from CO due to its high toxicity. Electrolysis of concentrated regolithic brines using an electrolyzer can be an alternate route to produce high-purity O_2. The oxygen evolution reaction (OER) at the anode of the electrolyzer is accompanied by the hydrogen evolution reaction (HER) at the cathode, thus producing fuel and oxidant in tandem that can be used as rocket propellant as well as life support, respectively. Given that the OER is slower (and hence rate limiting) compared to HER, we focus on OER electrocatalyst development for electrolyzers.

S3. Energy production on Mars

The very small amount of oxygen (0.14 %) present in the Martian atmosphere (10) has important biotic and geochemical implications (6). Further, the oxygen reduction reaction (ORR) in fuel cells is critical for energy production due to the inherent sluggishness of the ORR. Thus, the study of the ORR and electrocatalyst development for the same at Martian terrestrial conditions is also critical. Compton and co-workers investigated oxygen electrochemistry and transport properties in concentrated perchlorate brines at sub-zero temperatures while failing to simulate either the terrestrial pressure or atmospheric composition of Mars (6). We build on this ORR investigation by examining electrocatalysts in similar regolithic brine solutions under simulated

Martian temperatures and atmospheric conditions. Most importantly, we show that lead ruthenate pyrochlore serves as an excellent bifunctional ORR-OER electrocatalysts under Martian conditions.

S4. Oxygen evolution electrocatalysis in Martian environment

Low overpotential and high faradaic currents are the hallmarks of an efficient OER electrocatalyst. Metal oxides (e.g. perovskites, spinel oxides, layered double hydroxide (LDH) etc.) and non-metal oxides (e.g. metal chalcogenides, metal pnictides, organometallics, non-metals etc.) have been widely studied as OER electrocatalysts (11–15). RuO_2 and IrO_2 serve as OER electrocatalyst benchmarks due to their high activity and stability in both acidic and alkaline medium (16, 17). Amongst these candidates mentioned above, pyrochlores ($A_2B_2O_7$) exhibit high OER activity coupled with moderate ORR activity (18–21). This bifunctionality and moderate electrical conductivity has enabled its wide use in metal-air batteries, fuel cells and electrolyzers (19, 22–25). Pyrochlores exhibit high OER activity (10 mA cm^{-2} at ~200 mV overpotential) aided by their high electrical conductivity, high surface area (99 m^2 g^{-1}) and oxygen vacancy (19) that have enabled high performance (~800 mA cm^{-2} at 2 V) solid-state alkaline electrolyzer with concurrently high stability (19). Herein, we demonstrate for the first time that pyrochlores exhibit high OER activity in simulated Martian environment under near-neutral pH condition.

S5. Materials and Methods

S5.1. Synthesis of lead ruthenate pyrochlore

Lead ruthenate pyrochlores ($Pb_2Ru_2O_{7-\delta}$) were prepared by dissolving 5 mmol Ruthenium (III) nitrosylnitrate ($Ru(NO)(NO_3)_3$, Ru 31.3% minimum, Alfa Aesar) in 25 mL of DI water (18.2 MΩ cm) and stirred for 10 minutes. 5 mmol lead (II) nitrate ($Pb(NO_3)_2$, 99.999%, Sigma Aldrich) was also separately dissolved in 25 mL DI water and stirred for 10 minutes. The solutions were mixed and stirred for an additional 30 minutes. Subsequently, the mixture was added to 500 mL 4 M KOH solution and a precipitate was obtained. The precipitate was crystallized by maintaining the KOH solution at 85 ^oC with continuous oxygen bubbling for 5 days. The solution volume was maintained by adding DI water every 24 hours. Following 5 days of crystallization, the solid was separated by centrifugation (Thermo Scientific, Heraeus Multifuge X1) at 10000 rpm, with a subsequent centrifugal wash with DI water until pH 7-8 was achieved. Upon reducing the pH, the solid was further washed 3 times with glacial acetic acid followed by acetone (3 times) and dried at 60 ^oC overnight in an oven. The dry solid was ground and used for experiments.

S5.2. Analytical characterization

The electrical conductivity of $Pb_2Ru_2O_{7-\delta}$ was measured using a custom two-electrode conductivity cell consisting of two Cu solid rods encased in a hollow polyether ether ketone (PEEK) block (26). The powdered samples were placed between the Cu rods and compressed at a constant torque of 0.29 kg-m to ensure good electrical contact. The resistance (Ω, ohm) was calculated using electrochemical impedance spectroscopy (EIS) with a frequency range of 0.1-10^5 Hz with amplitude of 10 mV. The conductivity was measured according to the following formula:

$$\sigma = \frac{l}{R \times A} \quad \text{(S1)}$$

Where, σ is conductivity (S cm^{-1}), l is the sample thickness (cm), R is the measured resistance (ohm) and A is the cross-sectional area (cm^2).

The morphology of the samples and their elemental composition was examined using scanning electron microscopy (SEM) coupled with energy dispersive analysis of X-rays (EDAX) using a JEOL JSM-7001 LVF Field Emission SEM. Crystallographic characterization using X-ray diffraction (XRD) was carried out with a Bruker d8 advance x-ray diffractometer, scanning from 20 to 80º (2θ) at a rate of 0.5º $minute^{-1}$ followed by Rietveld refinement to determine the lattice constants. X-ray photoelectron spectroscopy (XPS) was performed on $Pb_2Ru_2O_{7-\delta}$ using 5000 VersaProbe II Scanning ESCA Microprobe with Al K-alpha x-ray source to determine the surface elemental composition and oxidation states. N_2 adsorption-desorption isotherms obtained using a QuantaChrome (QuantaSorb) instrument were analyzed using the Brunauer–Emmett–Teller (BET) model to determine the catalyst specific surface area.

S5.3. Experimental simulation of Martian environment

All experiments were performed in a simulated Martian environment. The low Martian terrestrial temperatures (-36 ^oC) were maintained by immersing the entire electrochemical experimental setup in a dry-ice bath with an ethylene glycol and ethanol mixture (27). By controlling the ratio of ethanol and ethylene glycol the temperature was lowered to -36 ^oC. The CO_2-rich Martian atmosphere was simulated by purging CO_2 into the electrolyte. All measurements were carried out in a 2.8 M $Mg(ClO_4)_2$ solution to mimic the anticipated liquid brine solutions on the Martian surface. Despite the low atmospheric pressure in Mars, we demonstrate that the regolithic brines remain in the liquid phase.

S5.4. Electrochemical measurements

The ORR and OER electrochemical activity of $Pb_2Ru_2O_{7-\delta}$ at various reaction regimes were evaluated using the standard rotating disk electrode (RDE) method (28). Catalyst inks were prepared by ultrasonication (QSonica; Q700 sonicator) of a mixture of 25 mg catalyst, 6 mL of 24 % (vol/vol) isopropanol/water, 0.275 mL of Nafion solution (Sigma Aldrich; 5 wt % solution in aliphatic alcohols) and 0.250 mL of 1 M KOH for 10 minutes (1 min. of sonication followed by 30 s cool down). KOH was added to neutralize the acidity of Nafion to preclude the possibility of $Pb_2Ru_2O_{7-\delta}$ exposure to acidic environments (29, 30).

Electrochemical measurements were carried out using a conventional three-electrode setup (Pine instruments, AKCELL). The working electrode (W.E.) consisted of a thin-film of 200 µg cm^{-2}_{disk} of $Pb_2Ru_2O_{7-\delta}$ supported on glassy carbon (GC). The W.E. was prepared by drop casting 10 µL of the $Pb_2Ru_2O_{7-\delta}$ ink onto a 0.196 cm^2 GC electrode polished to a mirror-like finish using 0.05 µm alumina slurry (Pine Instruments). The ink was dried in an uniform manner with homogenous particle distribution by rotating the RDE rotor at 400 rpm in an inverted position (31). Pt mesh and Ag wire were used as the counter and pseudo-reference electrode, respectively. Linear sweep voltammetry (LSV) was recorded by sweeping the potential at 20 mV s^{-1} in N_2-, O_2- and CO_2-saturated 2.8 M $Mg(ClO_4)_2$ electrolyte at different temperatures. The non-faradaic, capacitive current contributions were obtained from the scans under the N_2-saturated electrolyte.

The decision was made to employ an Ag wire pseudo-reference electrode (as opposed to standard reference electrodes like the Ag/AgCl reference) for the following reasons –

1. The temperature range of our studies (25ºC to -36ºC) means that the electrolyte in the Ag/AgCl electrode will freeze under some of these conditions. Further, the temperature range

means that there will be a significant difference in the potential of the Ag/AgCl electrode itself against the RHE.

2. The highly concentrated electrolyte we study increases the chance of contamination of the Ag/AgCl electrode as the concentration gradient will push our perchlorate electrolyte into the reference electrode. This contamination of the reference electrode's electrolyte will cause the potential of the Ag/AgCl electrode to shift against the RHE. Thus, it will no longer be a standard reference electrode.
3. The uncharacterized liquid junction potential when two concentrated and very different electrolytes are brough in contact at the reference electrode introduces significant uncertainties in the potential measured. Salt bridges also introduce similar uncertainty(32).

To remedy this common situation for studies involving highly concentrated electrolytes, high/low temperature electrochemistry and for non-aqueous solutions, IUPAC recommends the use of redox probes as an internal reference electrode wherein a well characterized redox couple is introduced into the electrolyte and the half-wave potential of this couple is used to calibrate potentials of our species of interest(33, 34).

We have calibrated the Ag reference electrode by adding potassium ferricyanide to the 2.8M $Mg(ClO_4)_2$ solution and measuring the half-wave potential of the standard ferricyanide/ferrocyanide redox couple (0.27 V vs. Ag wire (at pH=7); 0.71V vs. SHE (at pH=0)). Thus, given that $K_4Fe(CN)_6$ is well characterized in aqueous solutions (32, 35–38), this gives us an indirect way to tie the Ag wire reference potential to the SHE at pH=0. **Figure S2 (a)** depicts the relative potentials of the reversible hydrogen electrode (RHE), the Ag/AgCl electrode, the Ag wire pseudo-reference and the $Fe(CN)_6^{3-}$/ $Fe(CN)_6^{4-}$ internal redox probe calculated against the standard hydrogen electrode (SHE).

The pH dependence of the potential of the reversible hydrogen electrode is given by $\boldsymbol{E_0 = E_{0(pH=0,RTP)} - 0.059pH}$. Thus, at pH 7, the potential of the RHE is 0 - (0.059*7) = -0.413V vs. SHE. Further discussion and derivation of this equation can be found in *ACS Catalysis* 2020, 10, 8409−8417.

Similar conversions can be made for every reference electrode and redox couple when moving from one pH to another. Having found the difference between the $E_{1/2}$ of the ferricyanide/ferrocyanide couple when measured using a Ag wire vs the standard potential, we determined that the Ag wire exhibits a potential of 0.027 V vs SHE at pH = 7 and hence 0.44 V vs SHE at pH = 0. Thus, any potential reported in manuscript vs. Ag wire (at pH =7) can be converted to the value against SHE (at pH=0) by adding 0.44V for the reference electrode conversion and 0.413 for the pH conversion. Thus, a reading of 0.8V vs. Ag wire at pH=7 corresponds to 1.653 V vs. SHE at pH=0. The $E_{1/2}$ of the $Fe(CN)_6^{3-}$/ $Fe(CN)_6^{4-}$ redox couple and standard potentials of reference electrodes (both Ag wire and Ag/AgCl) varies with temperature, pH, concentration and nature of the electrolyte (e.g. chloride adsorption on the working electrode increases peak separation and shifts $E_{1/2}$ while perchlorate does not cause this effect (39)) we believe that the readers are best served by reporting the original data vs. Ag wire and enabling them to convert it to the SHE as needed for their specific conditions and applications.

Further, the stability of the Ag pseudo-reference electrode was confirmed by measuring the drift of the half-wave potential of the standard ferricyanide/ferrocyanide redox couple over time. No drift was observed confirming its stability as seen in **Figure S2(b)**.

Solution resistance was measured using EIS over the entire experimental temperature range and is depicted in **Figure S13**. Cathodic and anodic potential scans were carried out to measure the ORR and OER currents, respectively. All the LSV scans were corrected for resistive

and capacitive contributions. The measurements were carried out at different temperatures between 21 ºC to -36 ºC. The OER measurements were carried out under both O_2 and CO_2–saturated electrolytes while ORR was carried out only with O_2-saturated electrolyte.

S5.5. Solid-state Martian regolithic brine electrolyzer

The $Pb_2Ru_2O_{7-\delta}$ OER electrocatalyst was integrated into a 5 cm^2 single cell (Fuel Cell Technologies Inc.) solid-state alkaline water electrolyzer fed with CO_2 purged 2.8 M $Mg(ClO_4)_2$ operated at average Earth (21 ºC) and Martian terrestrial temperatures (-36 ºC). The laboratory setup is depicted in **Figure S15**. The anode bipolar plate was a corrosion-resistant titanium metal plate (2 × 2 mm^2 single parallel flow channels) to avoid carbon corrosion whereas cathode was a graphite plate (1 × 1 mm^2 three serpentine flow channels). Membrane electrode assembly (MEA) was fabricated by sandwiching an anion exchange membrane (AEM, Fumasep FAA-3-50, thickness = 50 μm) between two gas diffusion electrodes (GDE). GDEs were prepared by painting catalyst ink with a N_2-propelled airbrush (Badger 150) on gas diffusion layers (GDLs) consisting of carbon paper with high wettability on the cathode side and titanium sheet on anode side to avoid corrosion. For the anode, the $Pb_2Ru_2O_{7-\delta}$ ink was prepared by sonicating 0.05 g catalyst, 3.2 g isopropanol/water (1/1 vol %) and 0.176 g of 5 wt% solubilized AEM binder (Fumion FAA-3, Fumatech, properties listed in **Table S2**). For the cathode, the Pt/C catalyst (Pt 46.5%, Tanaka, Japan) ink was prepared by sonicating 0.05 g catalyst, 3.2 g isopropanol/water (1/1 vol%) and 0.428 g of 5 wt % solubilized AEM binder. This composition gives a catalyst to binder ratio of 85:15 and 70:30 for the anode and cathode, respectively. The $Pb_2Ru_2O_{7-\delta}$ loading was 1 mg cm^{-2} on the anode side whereas Pt/C loading was maintained as 0.5 mg_{Pt} cm^{-2} on the cathode side. The MEAs were ion-exchanged to the OH^- form by immersing the AEM and electrodes in three batches of 1 M KOH each for 8-10 hours for a total of 24-30 hours followed

by a thorough DI water wash (40). After the electrolyzer was assembled, 2.8 M $Mg(ClO_4)_2$ purged with CO_2 was fed to the electrolyzer at room temperature and Martian temperature (-36 ^oC) with a flow rate of 200 mL min^{-1}. A potential stair-step protocol was applied with the anodic sweep from 1.2 V to 2.2 V and the data was recorded following current relaxation after a 1 minute potentiostatic hold. The stability (overpotential loss) of the electrolyzer was tested by using a constant current hold at 400 mA cm^{-2} for 5 h. After the hold test, a potentiostatic hold (at 2.5 V) was applied for 30 min to the electrolyzer to recover the overpotential loss. The ionic conductivity of the separator was measured using potentiostatic electrochemical impedance spectroscopy (EIS). Potentiostatic EIS was chosen as galvanostatic EIS has been reported to result in inaccurate apparent separator resistance due to non-linear responses in the high frequency region (41). Galvanostatic EIS also leads to the formation of high resistance regions due to gas generation close to the separator in zero-gap electrolyzer cells (42). Potentiostatic EIS was measured following the protocols in Rodriguez *et al.* (41). The area specific resistance (ASR) and corresponding conductivity data over the operational temperature range is presented in **Figure S16**. The source Bode diagrams underpinning the resistance values are depicted in **Figure S17**. The ASR and conductivity values are lower than the manufacturer specification at room temperature. We attribute this to the lower ionic mobility of the perchlorate ion (compared to chloride ion) (43) in conjunction with the possible drying of the membrane when exposed to highly concentrated brine electrolytes

S6. Results and Discussions

S6.1. Analytical characterization

XRD measurements on freshly prepared samples confirmed the presence of Pb-Ru pyrochlore phases (**Figure S3**) when compared to the characteristic peaks of $Pb_2Ru_2O_{7-\delta}$ phases (JCPDS-ICDD = PDF-00-002-1365). The absence of additional peaks indicated the presence of high purity pyrochlore phases without any mixed oxide phases. The XRD peaks for $Pb_2Ru_2O_{7-\delta}$ did not match with that for RuO_2, confirming the absence of any RuO_2 phase. Rietveld refinement yielded lattice constants of a=b=c=10.325 **Å** in agreement with prior reports (19). The manifestly high crystallinity of the sample, attributable to extensive O_2-purging (5 days) at 85 ^oC obviated the need for further annealing (44).

Figure S4 depicts SEM micrographs indicating the formation of 70-140 nm spherical $Pb_2Ru_2O_{7-\delta}$ particles and the TEM images and particle size distribution of commercial RuO_2 and as-prepared $Pb_2Ru_2O_{7-\delta}$ pyrochlore sample are shown in Figure S4 (b) and (c). The size of the RuO_2 and $Pb_2Ru_2O_{7-\delta}$ particles are in the range of 21-37 nm and 5-12 nm, respectively. Both the samples are composed of tiny nanoparticles with high porosity and surface roughness leading to high surface area. The disparity in the particle size between SEM and TEM images can be attributed to sonication for the preparation of TEM samples. The formation of Pb-Ru-O system and the composition were confirmed by EDAX mapping (**Figure S5**). XPS of the samples detected the presence of multiple oxidation states of Pb, Ru and O in $Pb_2Ru_2O_{7-\delta}$. The atomic percentage of each species for $Pb_2Ru_2O_{7-\delta}$ is calculated from the XPS data to be: Pb = 18.8%, Ru = 18.5% and O = 62.7%. The deconvolution of O 1s spectrum yielded three distinct peaks at ~ 528.3 ± 0.2 eV, ~ 530 ± 0.1 eV and ~ 531 ± 0.5 eV corresponding to O-atoms in crystal lattice, auxiliary oxidation state of O-atom due to creation of oxygen vacancy and surface –OH state of O-atoms, respectively (**Figure S6a**). The deconvoluted Ru 3p XPS spectrum for $Pb_2Ru_2O_{7-\delta}$ showed the presence of two different oxidation states of Ru: Ru (IV) $3p_{3/2}$, Ru (V) $3p_{3/2}$, Ru (IV) $3p_{1/2}$ and

Ru (V) $3p_{1/2}$ at ~462.5 ± 0.4 eV, ~464.5 ± 0.4 eV, ~484.3 ± 0.2 eV and ~486.6 ± 0.3 eV, respectively (**Figure S6b**). Deconvolution of Pb 4f XPS peak shows the presence of Pb (II) $4f_{7/2}$, Pb (IV) $4f_{7/2}$, Pb (II) $4f_{5/2}$ and Pb (IV) $4f_{5/2}$ at ~136.2 ± 0.2 eV, ~137.3 ± 0.3 eV, ~141.3 ± 0.1 eV and ~142.2 ± 0.2 eV, respectively (**Figure S6c**). The deconvolution of the O 1s XPS peak for RuO_2 showed three sub-peaks at ~528.6 ± 0.3, ~530.1 ± 0.2 eV, and ~532.1 ± 0.2 eV, corresponding to lattice oxygen, surface hydroxyl groups, and adsorbed water. This was similar to prior literature studies (Figure S6d) (45). The data did not show the presence of any peak associated with oxygen vacancies in contrast to $Pb_2Ru_2O_{7-\delta}$. The deconvolution of the Ru 3p XPS peak showed a doublet with two sub-peaks at ~463.2 ± 0.2 eV, and ~485.2 ± 0.3, corresponding to Ru (IV) $3p_{3/2}$ and Ru (IV) $3p_{1/2}$, respectively, without any other Ru oxidation states. This was again in contrast to $Pb_2Ru_2O_{7-\delta}$, which was similar to previously reported data (Figure S6e) (46, 47). BET surface area of the $Pb_2Ru_2O_{7-\delta}$ sample was found to be 90 ± 4 m^2/g. The conductivity of $Pb_2Ru_2O_{7-\delta}$ sample has been calculated as 82 ± 4 S/cm.

S6.2. The thermodynamics of Martian regolithic brines

The low Martian atmospheric pressure, of ~6.4 mbar depresses the boiling point of pure water to -39.9 ^oC. This effect is countered in highly concentrated $Mg(ClO_4)_2$ brines where the high salt concentration elevates the boiling point. The boiling-point elevation can be calculated via following equation:

$$\Delta T_b = K_b b_B \quad \text{(S2)}$$

Where, ΔT_b is the elevation in boiling-point ($T_{b(solution)} - T_{b(pure\ solvent)}$), K_b is the ebullioscopic constant of pure solvent (0.512 for pure water), and b_B is molality of the solution. b_B can be calculated as $b_B = b_{solute} i$. Where, b_{solute} is the molarity of the solute and i is the van't Hoff factor

which is ~3 for $Mg(ClO_4)_2$. Equation S2 predicts a ΔT_b of 4.3 ^oC for 2.8 M $Mg(ClO_4)_2$, resulting in a boiling point of -35.6 ^oC. Therefore the perchlorate brine will neither freeze via freezing point depression nor vaporize/boil (vapor $pressure_{water@-40\ degC}$ = 0.39 mbar << 6.38 mbar = Martian atmospheric pressure) via boiling point elevation, allowing for the presence of liquid water solutions on the Martian surface.

The simulation of terrestrial Martian temperature accounted for the large diurnal temperature range, low atmospheric pressure and highly concentrated perchlorate brine. The low diurnal temperatures (-39 ^oC to -81 ^oC) suggested that water is most likely to be present in the solid/ice state. However, water present in highly concentrated perchlorate brines experiences a freezing point depression resulting a freezing temperature below -60 ^oC (6, 48). Therefore, spatiotemporal conditions exist on Mars to allow for the presence of liquid brine solutions. The extreme hygroscopic nature of perchlorate salts will also result in the absorption of atmospheric moisture even when present in very low concentrations of up to 210 ppm (49).

S6.3. Electrochemistry in simulated Martian environment

The OER activity of $Pb_2Ru_2O_{7-\delta}$ in O_2-purged simulated Martian regolithic brine (SMRB) was measured over a range of temperatures (21 ^oC to -36 ^oC) and benchmarked against RuO_2 and GC. $Pb_2Ru_2O_{7-\delta}$ exhibited higher OER currents (and hence OER activity) over the entire OER potential window compared to RuO_2 and GC at any temperature (**Figure S7**). **Figure S8** depicts the impact of the purged gases on the OER activity of $Pb_2Ru_2O_{7-\delta}$. The OER activity was unchanged between O_2 and CO_2 purged environment but the CO_2 purged SMRB exhibited <100 mV increase in the onset potential confirming minimal effect of gas environment. E vs. log j (Tafel) plots exhibited lower slopes for $Pb_2Ru_2O_{7-\delta}$ (144 – 155 mV dec^{-1}), demonstrating lower overpotentials/facile kinetics for OER compared to RuO_2 (187 – 225 $mVdec^{-1}$) and GC (331 –

600 mVdec^{-1}) electrode at 21 and -36 ^{o}C (**Figure S9a,b**). Tafel slopes (given by $b = -\frac{2.3RT}{\alpha F}$) close to 118 mV dec^{-1} indicates that the first electron transfer step is rate determining which confirms oxygen vacancy sensitive OER and the transfer coefficient (α) is 0.5, rendering both the forward and backward reaction equally facile (50–52). We have previously demonstrated the effect of the solvation shell on charge transfer at (or near) electrode surfaces (51, 53–55). The increasing Tafel slopes as a function of the temperature indicates an asymmetry in the overpotentials needed for the OER and ORR as the ORR is solvation controlled whereas OER is solvation independent as the solvent itself is the reactant (**Figure S9c,d**) (56). The Tafel slopes depicted in **Figure S9** are seen to be independent of the purge gas while the intercept varies in line with the onset potential from the LSVs. Temperature was found to have no influence on the mechanism as the Tafel slopes were unchanged with temperature. The expected drop in the reaction rate constant was evident in the decrease in the intercept and hence the exchange current density. The low Tafel slopes exhibited by $Pb_2Ru_2O_{7-\delta}$ indicate that α is closer to 0.5 and hence the energetics of the ORR and OER are facile, in line with our observations of bifunctional ORR/OER activity. The higher concentration of surface oxygen vacancies as well as higher oxidation states of surface Ru (Ru(IV) and Ru(V)) as confirmed by XPS (**Figure S6**) on $Pb_2Ru_2O_{7-\delta}$ as compared to RuO_2 (Ru(IV)) facilitate higher adsorption of water ($S + H_2O \rightarrow S\text{-}OH + H^+ + e^-$) to promote the first electron transfer, improving the OER activity analogous to Co_3O_4 electrocatalysts reported in the literature (23, 57).

Figure S10 depicts possible pathways for the reduction of O_2 in an acidic or near-neutral aqueous environment. The initial step in the ORR mechanism was considered to be the adsorption and subsequent reduction of oxygen to the superoxide radical. Outer sphere electron transfer (21) to form O_2^- and the possible subsequent adsorption of the superoxide radical was

also considered. The further electrochemical reduction of adsorbed O_2 (or O_2^-) by protons is dependent on the adsorption orientation of the oxygen species with end-on, side-on and bridge type adsorption being possibilities dictated by the nature of the electrode. Side-on adsorption is possible when the spacing between the catalytic active sites and the bond length of O_2 (or O_2^-) are similar. Talk about surface O_2 vacancies and the orientation renders an electrophilic H^+ attack on either O atom equally likely and offers the best possibility to follow a direct 4-electron pathway to produce H_2O. Alternatively, in end-on adsorption, the initial step is likely to be the formation of OOH species, followed by O-O bond cleavage and subsequent H^+ attack to produce $2OH^\bullet$ which further reacts to produce $2H_2O$. Alternatively, the formation of OOH maybe followed by the addition of another H^+ to produce H_2O_2. The H_2O_2 can further react with a series of H^+ ions to produce $2OH^\cdot$ and then $2H_2O$. The chemical decomposition of H_2O_2 to O_2 and the possible equilibriums in each of the steps in the mechanism are not considered due to the expected low concentration of H_2O_2 at the surface (due to constant convection during the rotation of the RDE) and the overpotential driving the reactions forward.

The ORR in the SMRB was examined at a range of temperatures, allowing us to establish the activity of the $Pb_2Ru_2O_{7-\delta}$ electrocatalysts and then translate it to the simulated Martian conditions to produce energy on Mars in future. Given the wide range of temperatures examined and the consequent increase in the overpotential required to initiate ORR, we have chosen to examine the activity of the catalysts at 200 mV overpotential at all temperatures with the overpotential chosen to improve the faradaic efficiency of the overall unitized regenerative fuel cell (URFC = electrolyzer and fuel cell) system. In **Figure S11**, the superior activity of $Pb_2Ru_2O_{7-\delta}$ compared to GC electrode is apparent at 21 ºC, with a 500mV lower ORR onset potential and ~3x the activity which is again attributed to high O_2 adsorption, subsequent

dissociation facilitated by high oxygen vacancy content (58). Given that GC is poor catalyst for the 4-electron ORR to produce H_2O, it exhibits minimal activity loss when the system is cooled from 21 ºC to -36 ºC. On the other hand, $Pb_2Ru_2O_{7-\delta}$ exhibit significant (~1/3 times) activity loss over the same temperature range. However, despite the activity loss, the pyrochlore electrocatalyst still exhibits an onset potential that is ~500mV lower than GC in a simulated Martian environment, providing a pathway to potential URFC development for energy and fuel production.

S6.4. Faradaic, voltage and energy efficiency

Faradaic efficiency is calculated using Faraday's law (equation S3) which states the relationship between the amount of charge (electron) transferred and number of moles reacted.

$$n_{ideal} = \frac{It}{Fz} \tag{S3}$$

$$Faradaic\ efficiency\ (FE) = \frac{n_{actual}}{n_{ideal}} \tag{S4}$$

Where, n_{ideal} = the number of moles of H_2/O_2 produced by the application of I, n_{actual} = the exact number of moles of H_2/O_2 produced, t = total time the measurement was taken for, I = total current applied, F = Faraday's constant (96485 C/mol) and z = total number of electrons transferred for H_2/O_2 production. Faradaic losses/efficiencies are calculated to check the energy losses as heat and/or by-product formation.

The voltage efficiency of our electrolyzer is calculated according to the following equation (59):

$$Voltage\ efficiency\ (VE) = \frac{Thermo-neutral\ voltage}{Cell\ operating\ voltage} \tag{S5}$$

Thermo-neutral voltage at -36 ^{0}C is calculated as 1.49 V according to the literature (60).

The energy efficiency of the electrolyzer is also calculated according to the following equation (61):

$$Energy\,efficiency\,(EE) = FE_{H_2/O_2} \times \left[E^0_{O_2,H_2O} - E^0_{H_2,H_2O} \right] / E_{cell} \quad \text{(S6)}$$

Where, $FE_{H2/O2}$ is faradaic efficiency at a given cell voltage, $E^0_{O2,H2O}$ and $E^0_{H2,H2O}$ are the standard potentials for oxygen and hydrogen production, respectively, and E_{cell} is the operating cell voltage.

The FE, VE and EE are calculated at 21 ^{0}C for the electrolyzer to be in the range of 64 – 74%, 68 – 99% and 36 – 60%, respectively. At -36 ^{0}C, our electrolyzer shows FE, VE and EE to be in the range of 65 – 75%, 68 – 100% and 37 – 56%, respectively.

References

1. Boynton W V., et al. (2001) Thermal and Evolved Gas Analyzer: Part of the Mars Volatile and Climate Surveyor integrated payload. *J Geophys Res E Planets* 106(E8):17683–17698.
2. Hecht MH, et al. (2009) Microscopy capabilities of the microscopy, electrochemistry, and conductivity analyzer. *J Geophys Res E Planets* 114(3):1–28.
3. Kounaves SP, et al. (2010) Soluble sulfate in the martian soil at the Phoenix landing site. *Geophys Res Lett* 37(9):1–5.
4. Wadsworth J, Cockell CS (2017) Perchlorates on Mars enhance the bacteriocidal effects of UV light. *Sci Rep* 7(1):1–8.

5. Smith PH, et al. (2009) H $_2$ O at the Phoenix Landing Site. *Science (80-)* 325(5936):58–61.

6. Elliott J, Ngamchuea K, Batchelor-Mcauley C, Compton RG (2017) Martian Redox Chemistry: Oxygen Reduction in Low-Temperature Magnesium Perchlorate Brines. *J Phys Chem Lett* 8(24):6171–6175.

7. Lauro SE, et al. (2020) Multiple subglacial water bodies below the south pole of Mars unveiled by new MARSIS data. *Nat Astron*. doi:10.1038/s41550-020-1200-6.

8. Landis GA, et al. (2017) Design Study of a Mars Ascent Vehicle for Sample Return Using In-Situ Generated Propellant. (January):1–12.

9. Weinstock M (2020) Oxygen-creating instrument selected to fly on the upcoming Mars 2020 mission. (August 2014):1–3.

10. NASA (2019) Mars Fact Sheet. *Natl Aeronaut Sp Adm*:5–8.

11. Suen N-T, et al. (2017) Electrocatalysis for the oxygen evolution reaction: recent development and future perspectives. *Chem Soc Rev* 46(2):337–365.

12. Seitz LC, et al. (2016) A highly active and stable IrOx/SrIrO3catalyst for the Oxygen evolution reaction. *Science (80-)* 353(6303):1011–1014.

13. Li P, et al. (2019) Boosting oxygen evolution of single-atomic ruthenium through electronic coupling with cobalt-iron layered double hydroxides. *Nat Commun* 10(1):1–11.

14. Chen G, et al. (2017) Nanofilms With Tunable Oxidation State. *Sci Adv* (June):1–9.

15. Mohammed-Ibrahim J, Xiaoming S (2019) Recent progress on earth abundant electrocatalysts for hydrogen evolution reaction (HER) in alkaline medium to achieve efficient water splitting – A review. *J Energy Chem* 400(July):111–160.

16. Lee Y, Suntivich J, May KJ, Perry EE, Shao-Horn Y (2012) Synthesis and activities of

rutile IrO 2 and RuO 2 nanoparticles for oxygen evolution in acid and alkaline solutions. *J Phys Chem Lett* 3(3):399–404.

17. McCrory CCL, Jung S, Peters JC, Jaramillo TF (2013) Benchmarking heterogeneous electrocatalysts for the oxygen evolution reaction. *J Am Chem Soc* 135(45):16977–16987.
18. Horowitz HS (2006) Oxygen Electrocatalysis on Some Oxide Pyrochlores. *J Electrochem Soc* 130(9):1851.
19. Parrondo J, George M, Capuano C, Ayers KE, Ramani V (2015) Pyrochlore electrocatalysts for efficient alkaline water electrolysis. *J Mater Chem A* 3(20):10819–10828.
20. Manoharan R, Goodenough JB (1995) Oxygen reduction on CrO2 bonded to a proton-exchange membrane. *Electrochim Acta* 40(3):303–307.
21. Prakash J, Tryk D, Yeager E (1990) Electrocatalysis for oxygen electrodes in fuel cells and water electrolyzers for space applications. *J Power Sources* 29(3–4):413–422.
22. Oh SH, Black R, Pomerantseva E, Lee JH, Nazar LF (2012) Synthesis of a metallic mesoporous pyrochlore as a catalyst for lithium-O 2 batteries. *Nat Chem* 4(12):1004–1010.
23. Park J, et al. (2017) Single crystalline pyrochlore nanoparticles with metallic conduction as efficient bi-functional oxygen electrocatalysts for Zn-air batteries. *Energy Environ Sci* 10(1):129–136.
24. Zen J-M (2006) Oxygen Reduction on Ruthenium-Oxide Pyrochlore Produced in a Proton-Exchange Membrane. *J Electrochem Soc* 141(4):L51.
25. Bae JM, Steele BCH (1999) Properties of pyrochlore ruthenate cathodes for intermediate temperature solid oxide fuel cells. *J Electroceramics* 3(1):37–46.

26. Kumar A, Ramani VK (2013) RuO2-SiO2 mixed oxides as corrosion-resistant catalyst supports for polymer electrolyte fuel cells. *Appl Catal B Environ* 138–139:43–50.

27. Jensen CM, Lee DW (2009) Dry-Ice Bath Based on Ethylene Glycol Mixtures. *J Chem Educ* 77(5):629.

28. Suntivich J, et al. (2011) Design principles for oxygen-reduction activity on perovskite oxide catalysts for fuel cells and metal-air batteries. *Nat Chem* 3(7):546–550.

29. Lin Y, et al. (2019) Chromium-ruthenium oxide solid solution electrocatalyst for highly efficient oxygen evolution reaction in acidic media. *Nat Commun* 10(1). doi:10.1038/s41467-018-08144-3.

30. Kim J, et al. (2017) High-Performance Pyrochlore-Type Yttrium Ruthenate Electrocatalyst for Oxygen Evolution Reaction in Acidic Media. *J Am Chem Soc* 139(34):12076–12083.

31. Garsany Y, Singer IL, Swider-Lyons KE (2011) Impact of film drying procedures on RDE characterization of Pt/VC electrocatalysts. *J Electroanal Chem* 662(2):396–406.

32. Murray RC, Rock PA (1968) The determination of the ferrocyanide-ferricyanide standard electrode potential at 25°C in cells without liquid junction using cation-sensitive glass electrodes. *Electrochim Acta* 13(4):969–975.

33. Pingarrón JM, et al. (2020) Terminology of electrochemical methods of analysis (IUPAC Recommendations 2019). *Pure Appl Chem* 92(4):641–694.

34. Gritzner G, Kuta J (1984) Recommendations on reporting electrode potentials in nonaqueous solvents (Recommendations 1983). *Pure Appl Chem* 56(4):461–466.

35. Lewis GN, Sargent LW (1909) THE POTENTIAL OF THE FERRO-FERRICYANIDE ELECTRODE. *J Am Chem Soc* 31(3):355–363.

36. Kolthoff IM, Tomsicek WJ (1935) The Oxidation Potential of the System Potassium Ferrocyanide–Potassium Ferricyanide at Various Ionic Strengths. *J Phys Chem* 39(7):945–954.

37. Rock PA (1966) The standard oxidation potential of the ferrocyanide-ferricyanide electrode at 25° and the entropy of ferrocyanide ion. *J Phys Chem* 70(2):576–580.

38. Peter LM, Dürr W, Bindra P, Gerischer H (1976) The influence of alkali metal cations on the rate of the Fe(CN)64−/Fe(CN)63− electrode process. *J Electroanal Chem Interfacial Electrochem* 71(1):31–50.

39. Wu CD, Calvo EJ, Yeager E (1983) Electrochemical Studies of Redox Systems for Energy Storage. *Nasa Cr-174503* (Ii).

40. Varcoe JR, et al. (2014) Anion-exchange membranes in electrochemical energy systems. *Energy Environ Sci* 7(10):3135–3191.

41. Rodríguez J, et al. (2019) Simple and precise approach for determination of Ohmic contribution of diaphragms in alkaline water electrolysis. *Membranes (Basel)* 9(10). doi:10.3390/membranes9100129.

42. Stojadinovic J, et al. (2012) Electrochemical characterization of porous diaphragms in development for gas separation. *ECS Electrochem Lett* 1(4). doi:10.1149/2.002204eel.

43. Aoki K (2004) An interpretation of small values of the transfer coefficient at conducting polymers. *J Electroanal Chem* 569(1):121–125.

44. Prakash J, Tryk DA, Aldred W, Yeager EB, Reserve CW (1999) Investigations of ruthenium pyrochlores as bifunctional oxygen electrodes. 1463–1469.

45. Wang W, et al. (2014) Hydrous ruthenium oxide nanoparticles anchored to graphene and carbon nanotube hybrid foam for supercapacitors. *Sci Rep* 4(ii):9–14.

46. Wang P, Liu H, Tan Q, Yang J (2014) Ruthenium oxide-based nanocomposites with high specific surface area and improved capacitance as a supercapacitor. *RSC Adv* 4(81):42839–42845.

47. Gayen P, Saha S, Ramani V (2020) Selective Seawater Splitting Using Pyrochlore Electrocatalyst. *ACS Appl Energy Mater*. doi:10.1021/acsaem.0c00383.

48. Pestova ON, Myund LA, Khripun MK, Prigaro A V (2005) PHYSICOCHEMICAL STUDIES OF SYSTEMS AND PROCESSES Study and Thermodynamic Analysis of the ZrO 2 SiO 2 System. *Russ J Appl Chem* 78(3):409–413.

49. Williams DR (2018) Mars Fact Sheet. *NASA Sp Sci Data Coord Arch*. Available at: https://nssdc.gsfc.nasa.gov/planetary/factsheet/marsfact.html [Accessed February 7, 2019].

50. Prakash, Jai; Tryk, Donald A; Yeager E (1999) Kinetic Investigations of Oxygen Reduction and Evolution Reactions on Lead Ruthenate Catalysts. *J Electrochem Soc* 146(11):4145.

51. Sankarasubramanian S, Seo J, Mizuno F, Singh N, Prakash J (2017) Elucidating the Oxygen Reduction Reaction Kinetics and the Origins of the Anomalous Tafel Behavior at the Lithium-Oxygen Cell Cathode. *J Phys Chem C* 121(9):4789–4798.

52. Bard AJ, Faulkner LR (2000) *Electrochemical Methods: Fundamentals and Applications* (Wiley). 2nd Ed. doi:10.1016/B978-0-12-381373-2.00056-9.

53. Li Y, Parrondo J, Sankarasubramanian S, Ramani V (2019) Impact of Surface Carbonyl- and Hydroxyl-Group Concentrations on Electrode Kinetics in an All-Vanadium Redox Flow Battery. *J Phys Chem C* 123(11):6370–6378.

54. Sankarasubramanian S, Kahky J, Ramani V (2019) Tuning anion solvation energetics

enhances potassium–oxygen battery performance. *Proc Natl Acad Sci U S A* 116(30):14899–14904.

55. Sankarasubramanian S, Ramani V (2018) Dimethyl Sulfoxide-Based Electrolytes for High-Current Potassium–Oxygen Batteries. *J Phys Chem C* 122(34):acs.jpcc.8b03755.

56. Fang YH, Liu ZP (2014) Tafel kinetics of electrocatalytic reactions: From experiment to first-principles. *ACS Catal* 4(12):4364–4376.

57. Zhang JJ, et al. (2017) Oxygen Vacancy Engineering of Co3O4 Nanocrystals through Coupling with Metal Support for Water Oxidation. *ChemSusChem* 10(14):2875–2879.

58. Cheng F, et al. (2013) Enhancing electrocatalytic oxygen reduction on MnO 2 with vacancies. *Angew Chemie - Int Ed* 52(9):2474–2477.

59. Harrison KW, Remick R, Martin GD, Hoskin A (2010) Hydrogen Production : Fundamentals and Case Study Summaries.

60. Mržljak M, Drobnič T, Sekavčnik B (2013) Integral Characteristics of Hydrogen Production in Alkaline Electrolysers. *J Mech Eng* 59:585–594.

61. Tatin A, Comminges C, Kokoh B, Costentin C, Robert M (2016) Efficient electrolyzer for CO 2 splitting in neutral water using earth-abundant materials. *Proc Natl Acad Sci* 113:5526–5529.

62. David R. Williams (2019) Earth Fact Sheet. *NASA Sp Sci Data Coord Arch*:1.

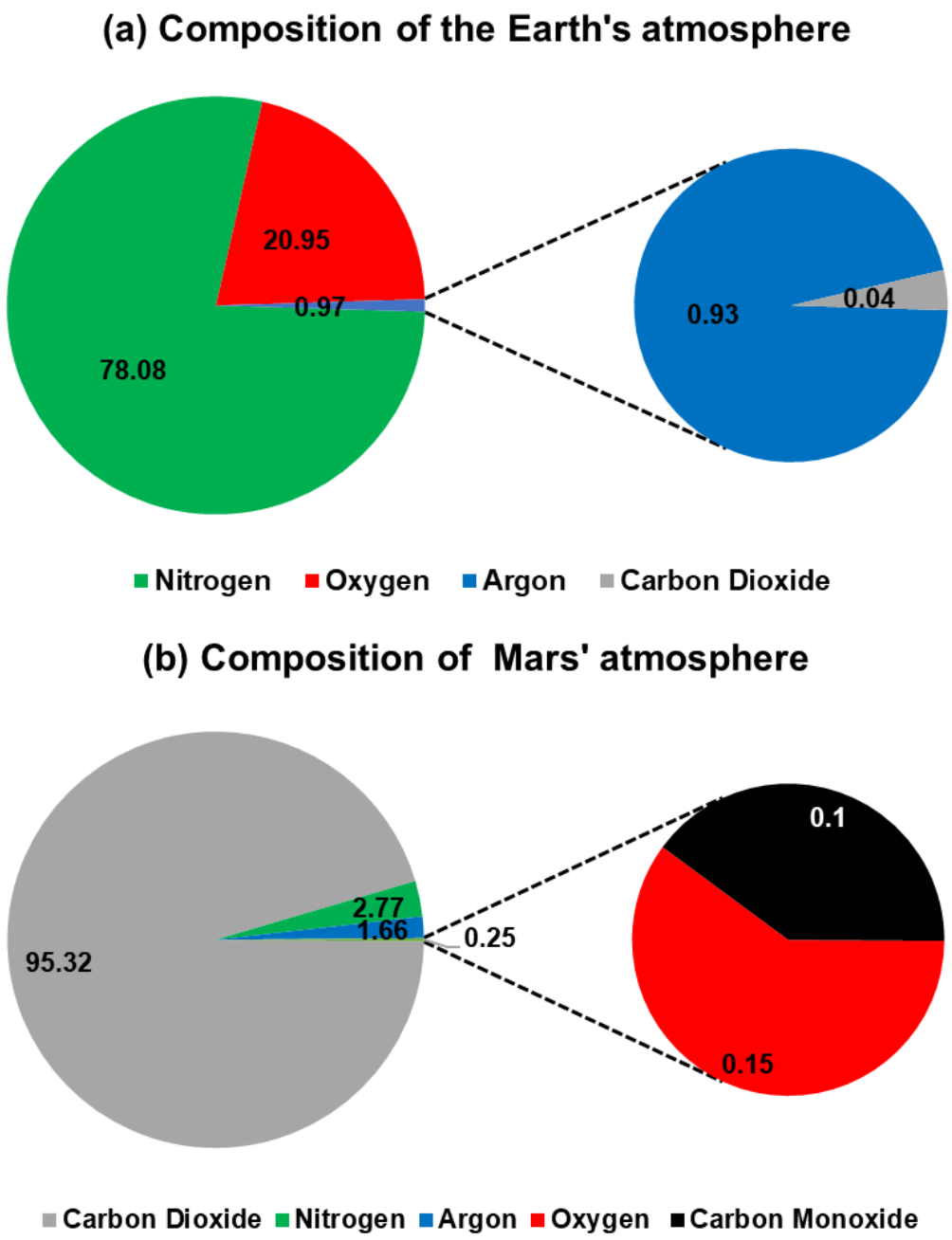

Figure S1. Comparison of the major constituents of the atmospheres of **(a)** Earth(62) and **(b)** Mars.(49) Transient species such as water vapor are not depicted.

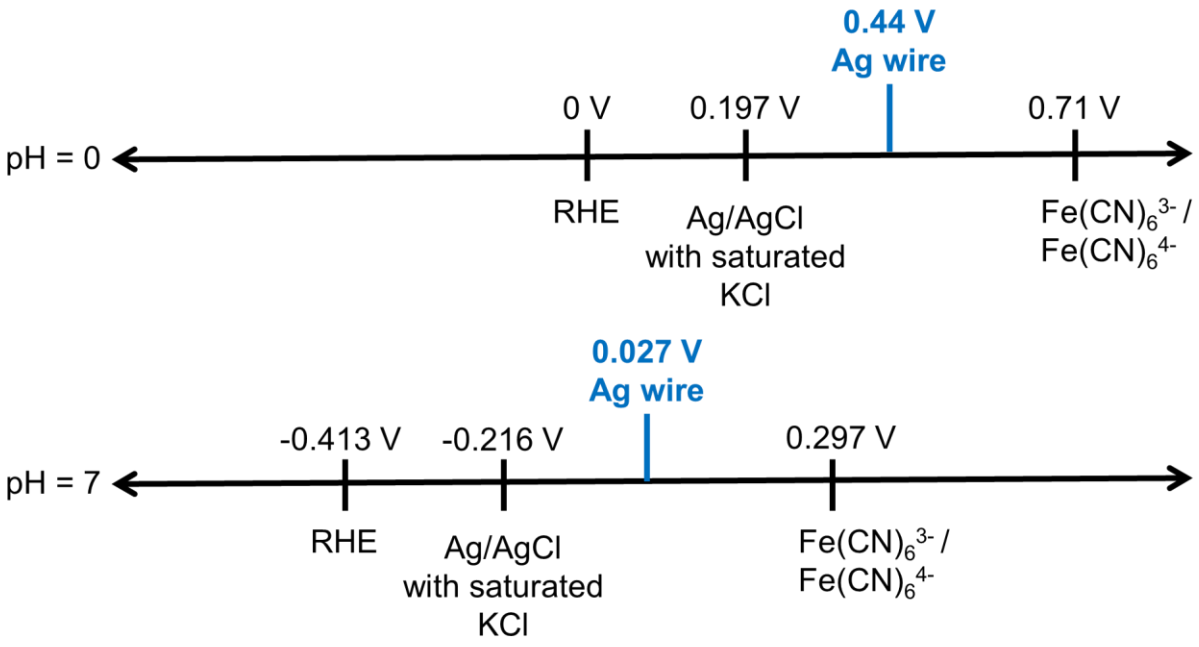

(a)

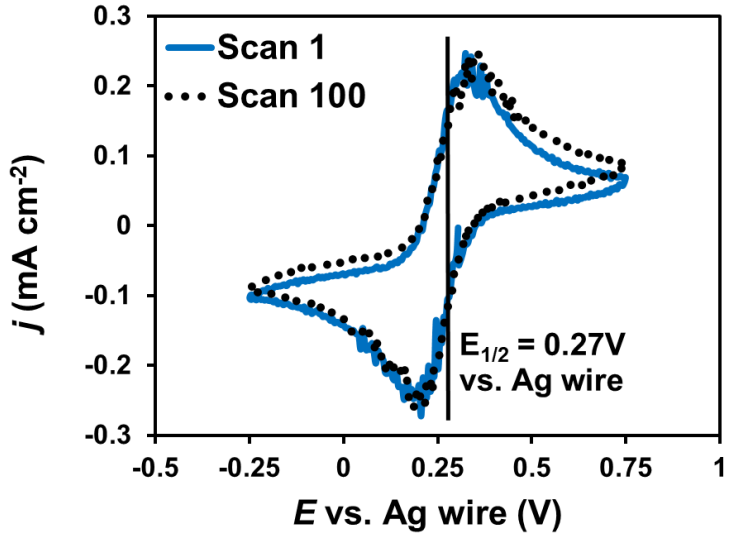

(b)

Figure S2. (a) Relative positions of the RHE, Ag/AgCl, Ag wire and ferricyanide/ferrocyanide redox couple at pH=0 and pH=7, **(b)** stability of the Ag wire pseudo-reference.

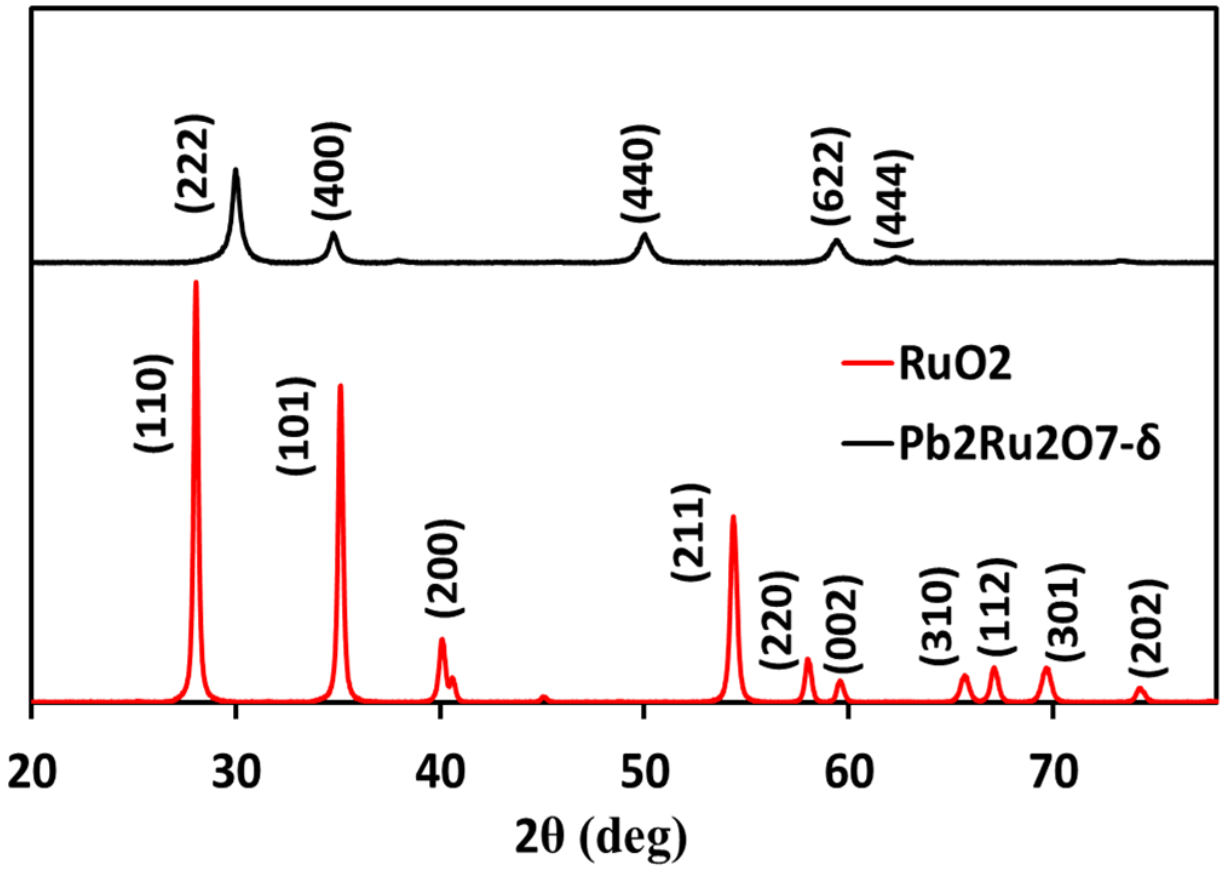

Figure S3. XRD spectra of as-prepared $Pb_2Ru_2O_{7-\delta}$ pyrochlore and commercial RuO_2 sample.

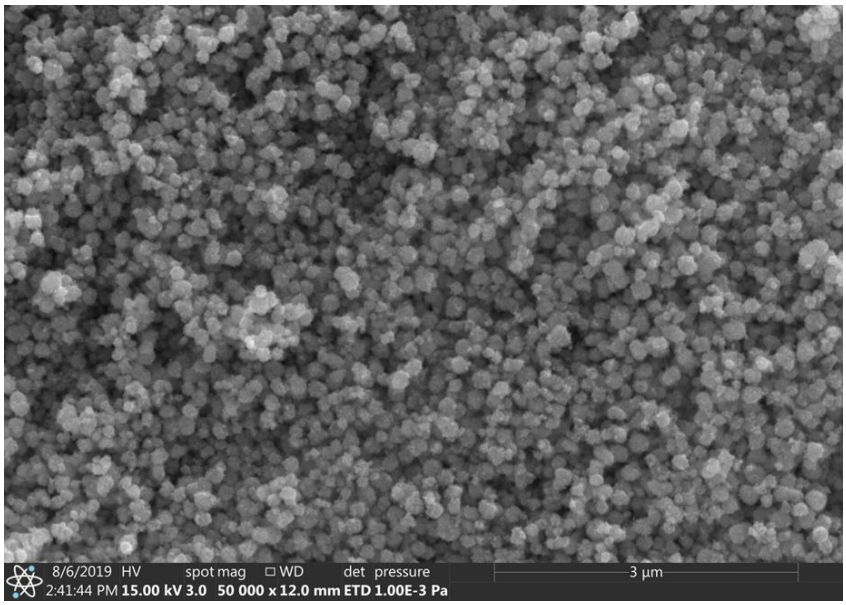

(a)

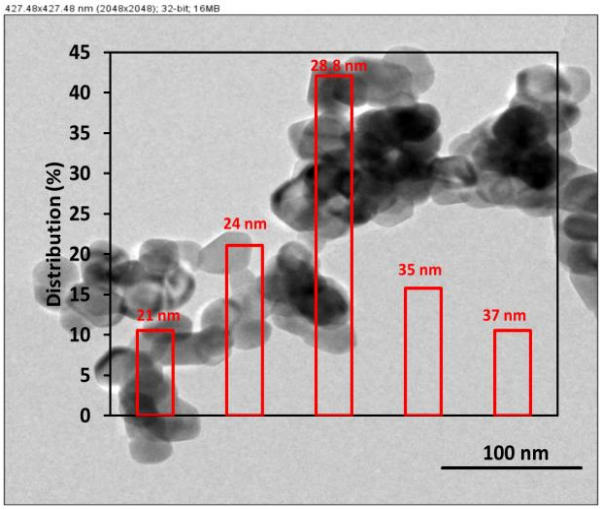

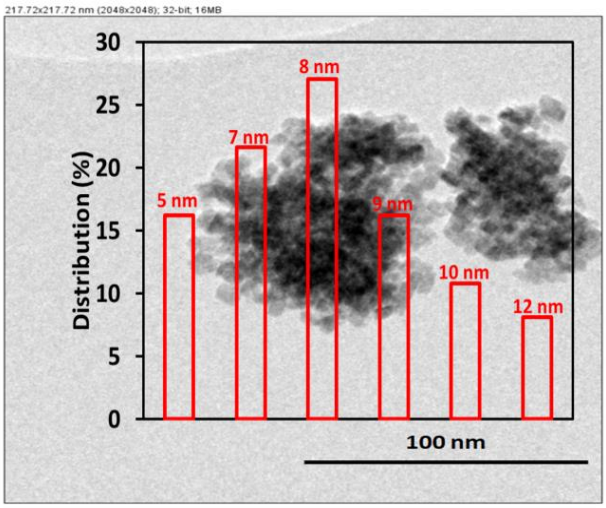

(b) **(c)**

Figure S4. Electron microscopy **(a)** SEM of as-prepared $Pb_2Ru_2O_{7-\delta}$ sample, TEM images of **(b)** commercial RuO_2 and **(c)** as-prepared $Pb_2Ru_2O_{7-\delta}$ pyrochlore sample.

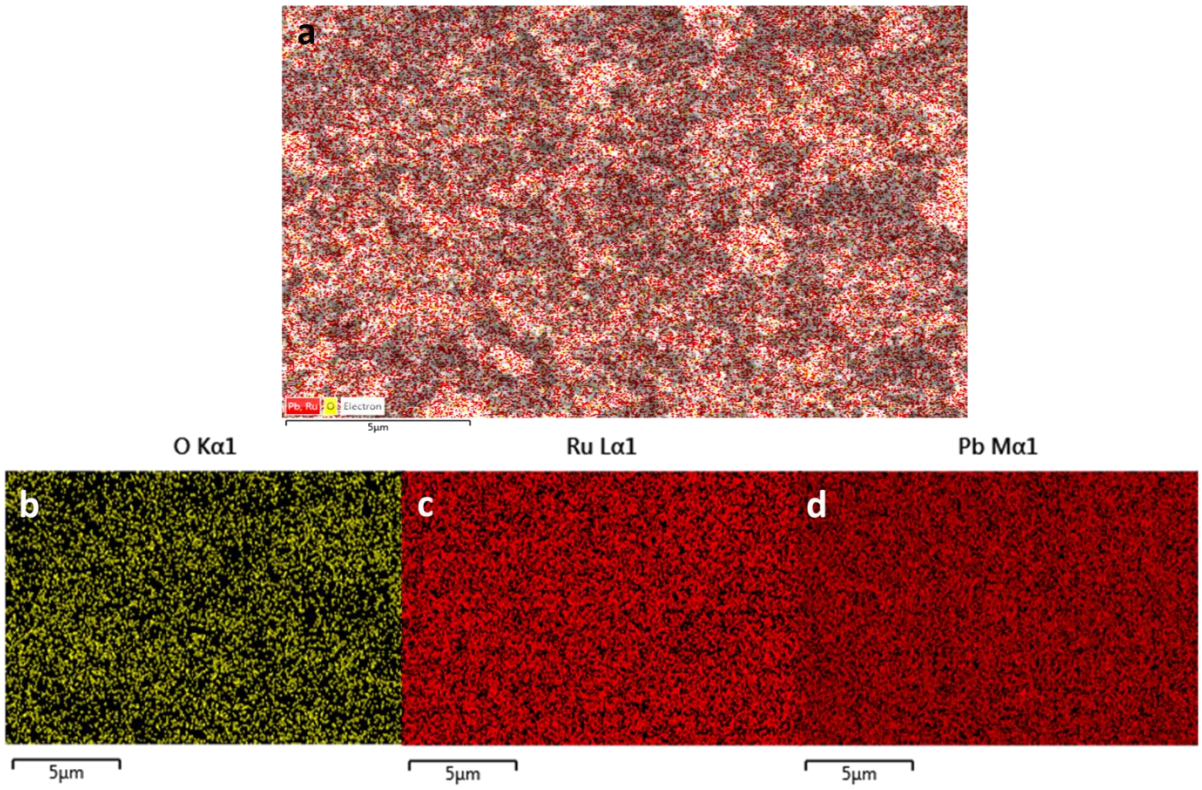

Figure S5. a) Layered EDAX of as-prepared pyrochlore sample. EDAX elemental mapping of b) O, c) Ru and d) Pb in pyrochlore.

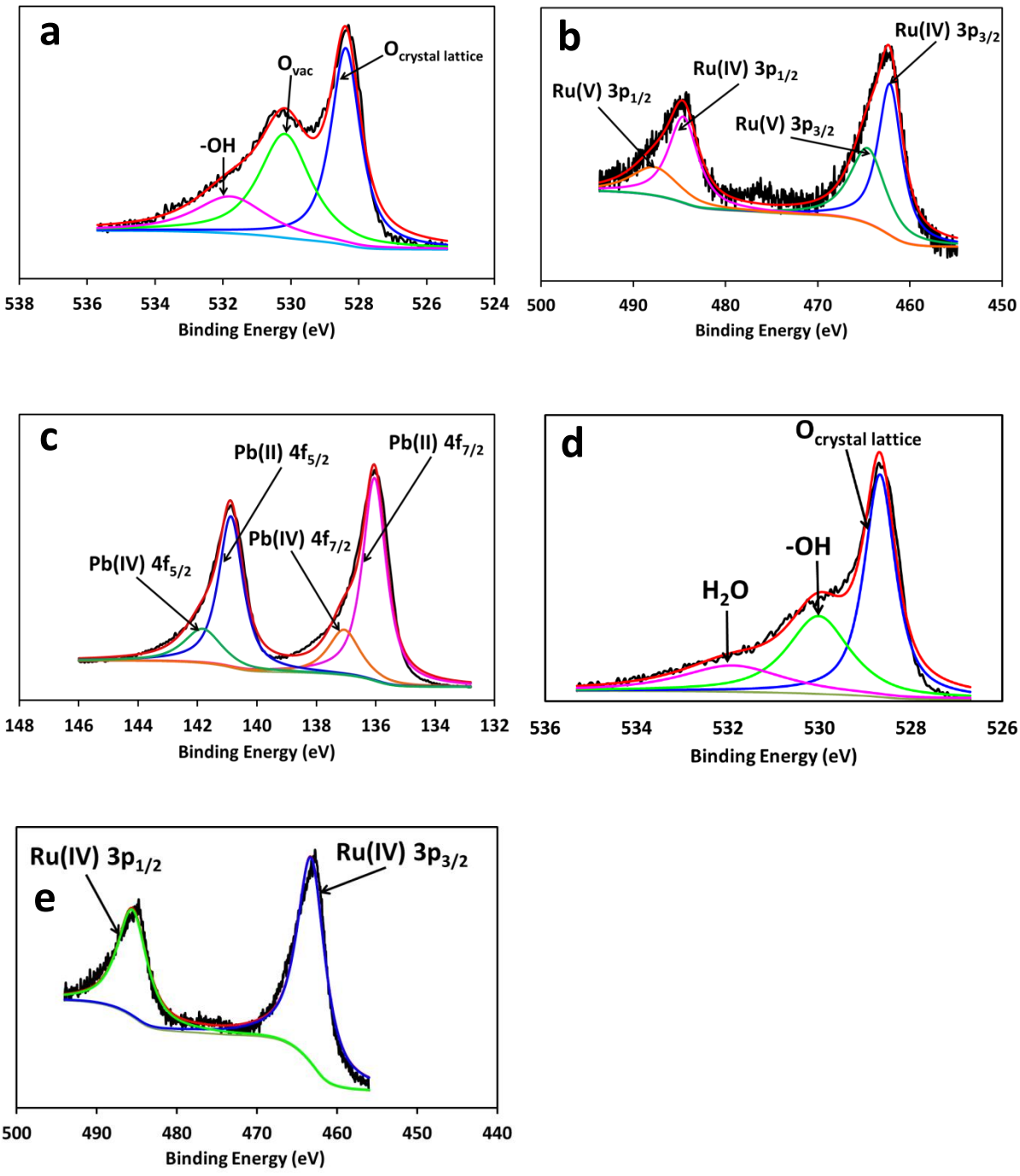

Figure S6. XPS of a) O 1s, b) Ru 3p and c) Pb 4f regions of $Pb_2Ru_2O_{7-\delta}$, d) O 1s and e) Ru 3p of RuO_2.

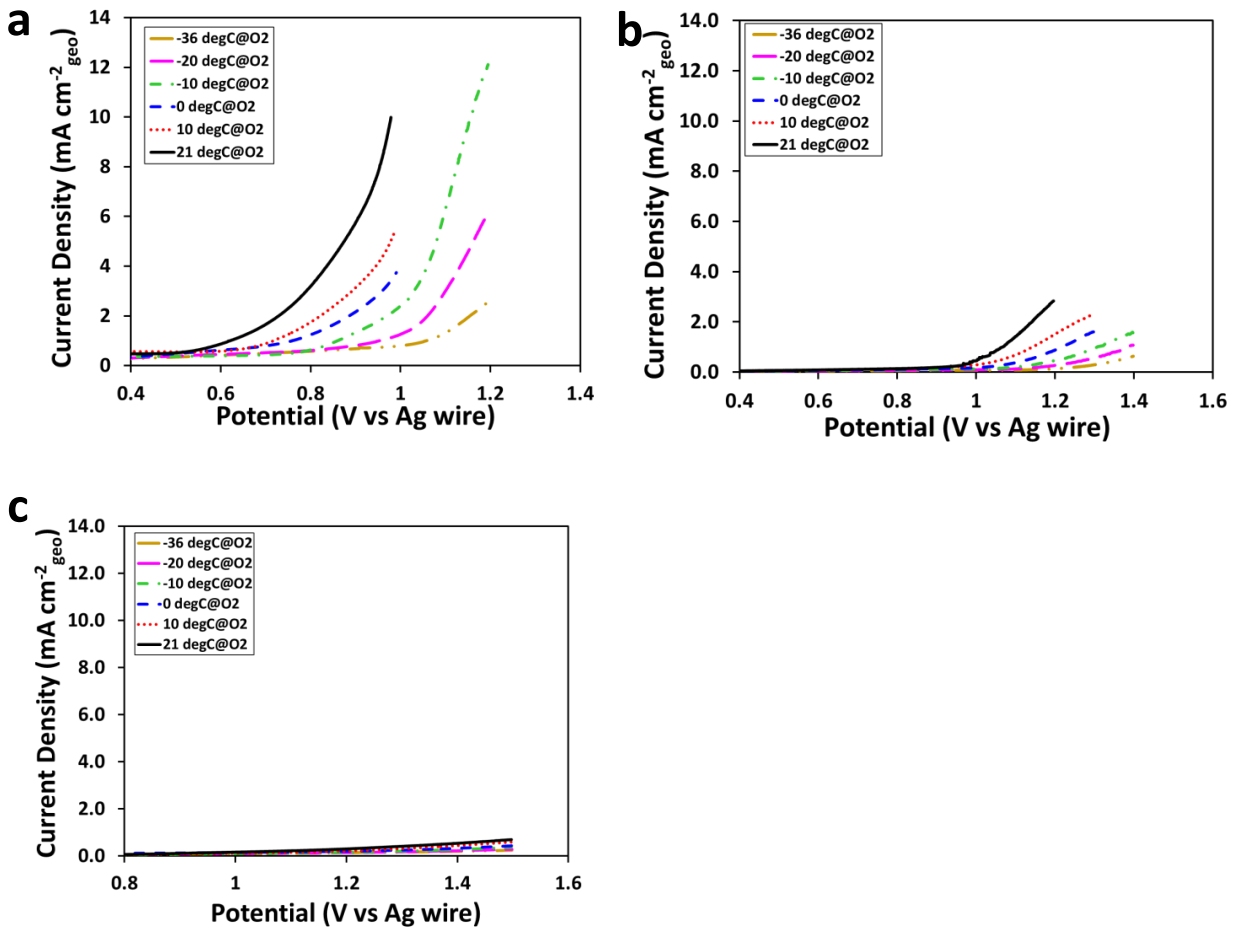

Figure S7. OER LSV curves for a) $Pb_2Ru_2O_{7-\delta}$, b) RuO_2 and c) GC under O_2-purged SMRB over a range of temperatures (21 ^oC to -36 ^oC).

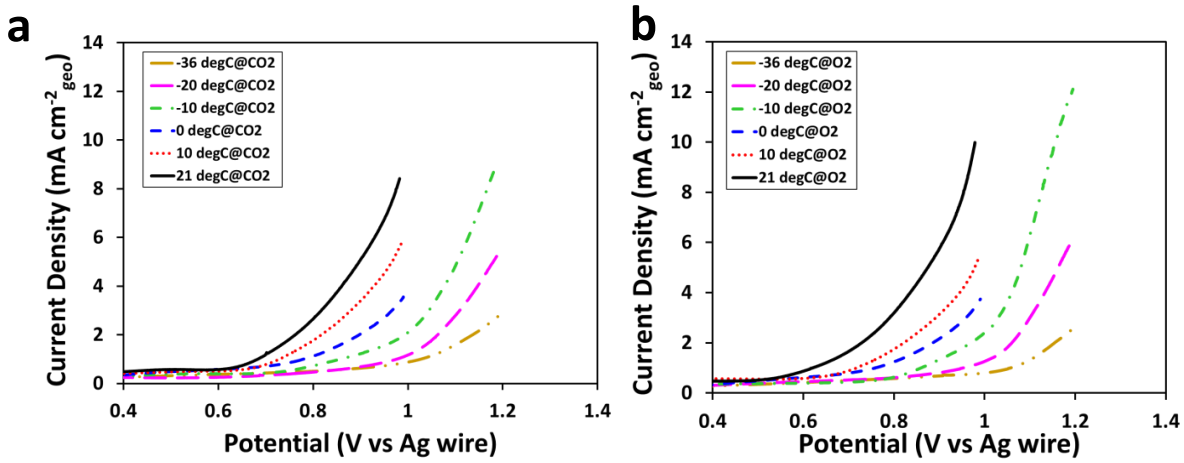

Figure S8. OER LSV curves for $Pb_2Ru_2O_{7-\delta}$ under a) CO_2-purged and b) O_2-purged SMRB over a range of temperatures (21 ^oC to -36 ^oC).

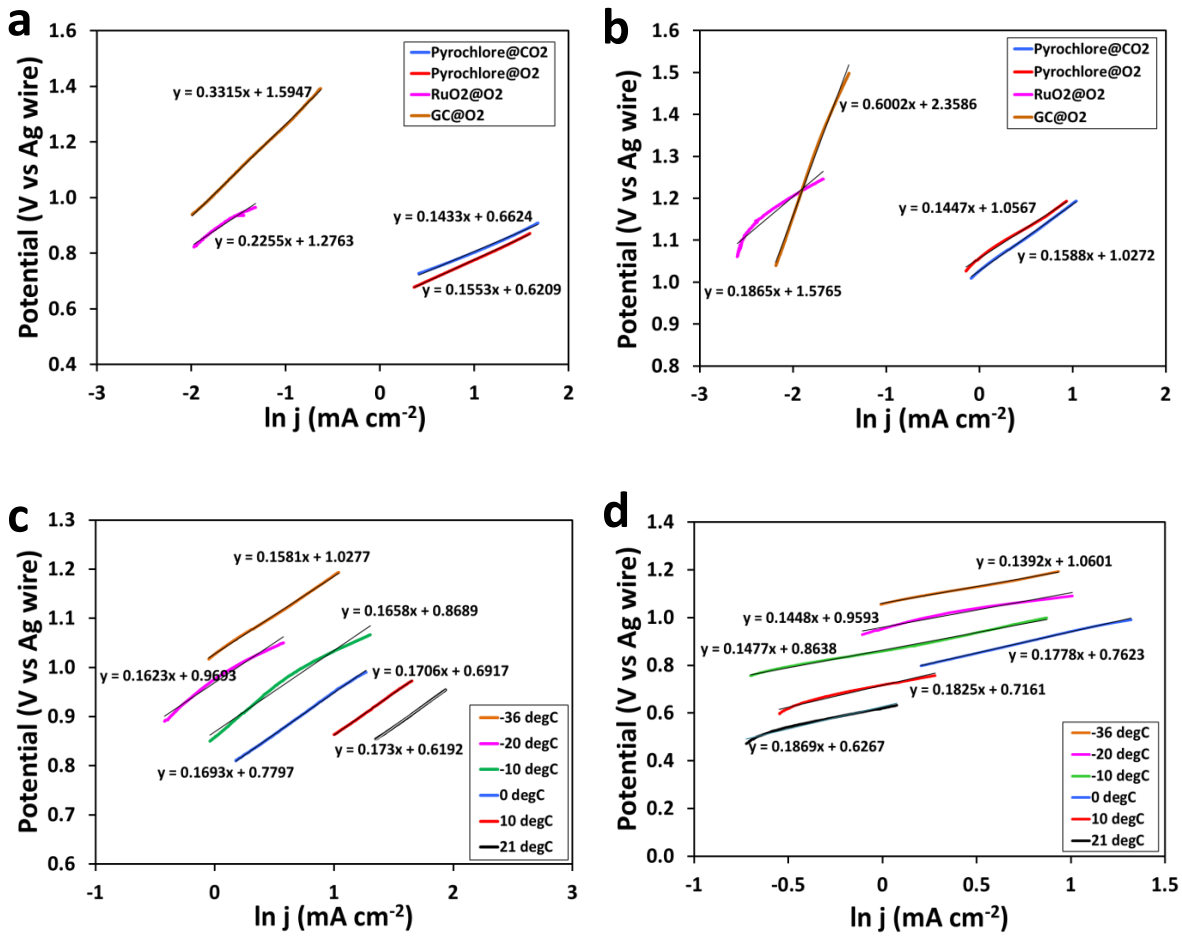

Figure S9. Tafel slopes of $Pb_2Ru_2O_{7-\delta}$, RuO_2 and GC under O_2- and CO_2-purged SMRB at a) 21 ^oC and b) -36 ^oC. c) Tafel slopes of $Pb_2Ru_2O_{7-\delta}$ under c) CO_2-purged and d) O_2-purged SMRB at different temperatures.

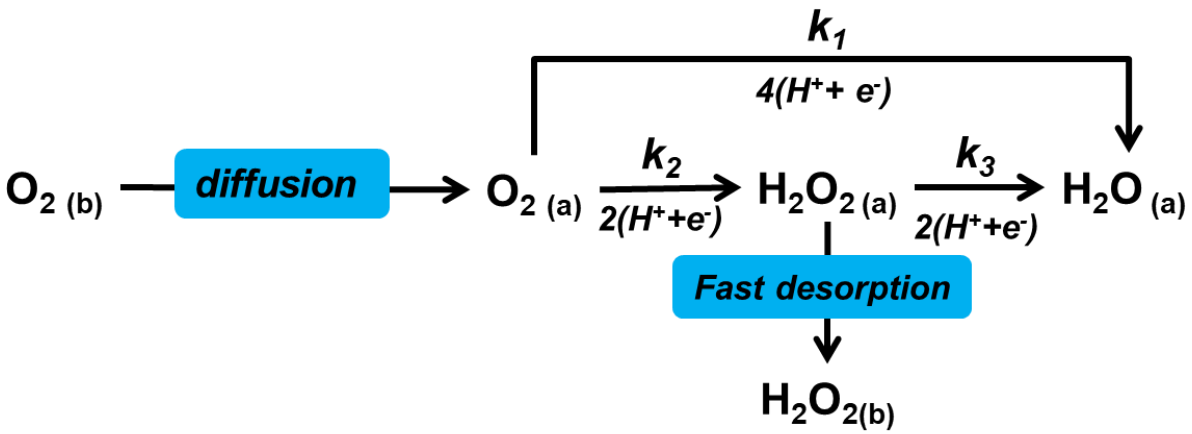

Figure S10. Reaction scheme for the ORR in acidic and near-neutral environments.

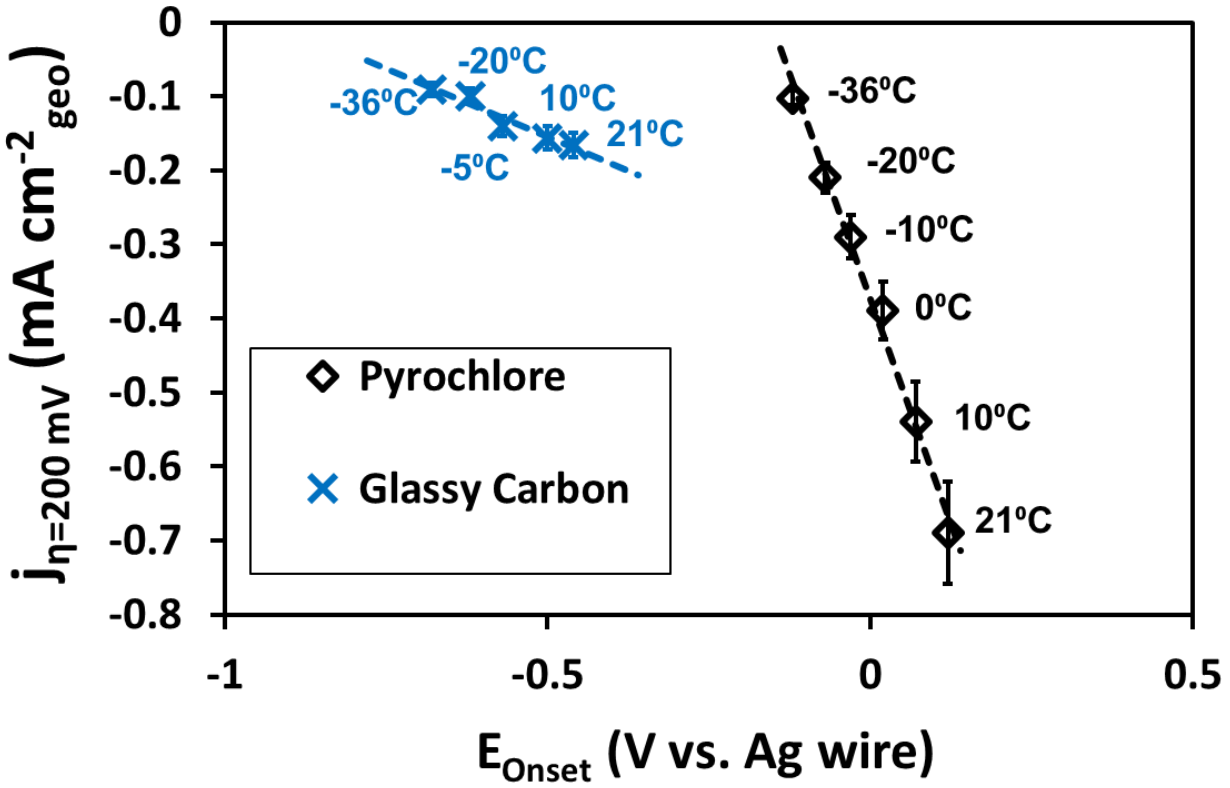

Figure S11. ORR current density at 200 mV overpotential vs. onset potential for $Pb_2Ru_2O_{7-\delta}$ and GC at O_2-purged SMRB at different temperatures.

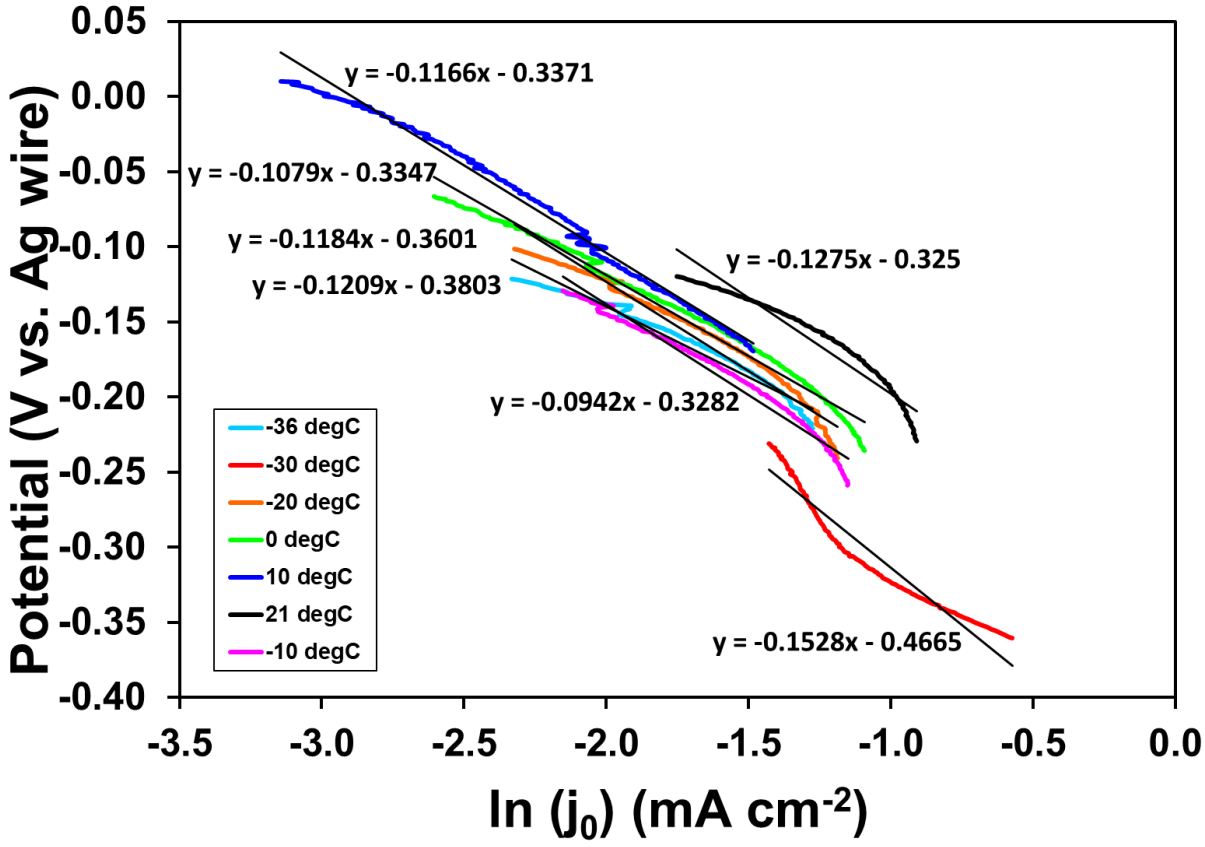

Figure S12. Tafel slopes for HER with Pt/C in CO_2-purged SMRB at different temperatures.

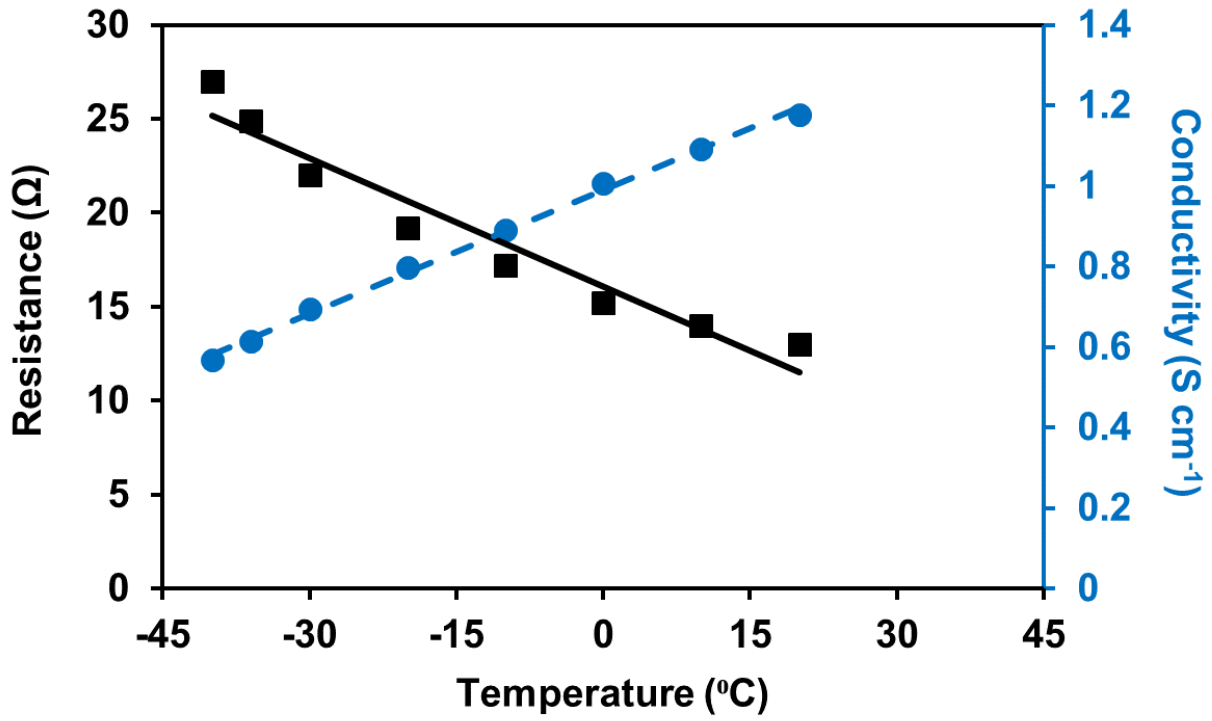

Figure S13. The resistance and conductivity measurements of the electrolyte at different temperatures.

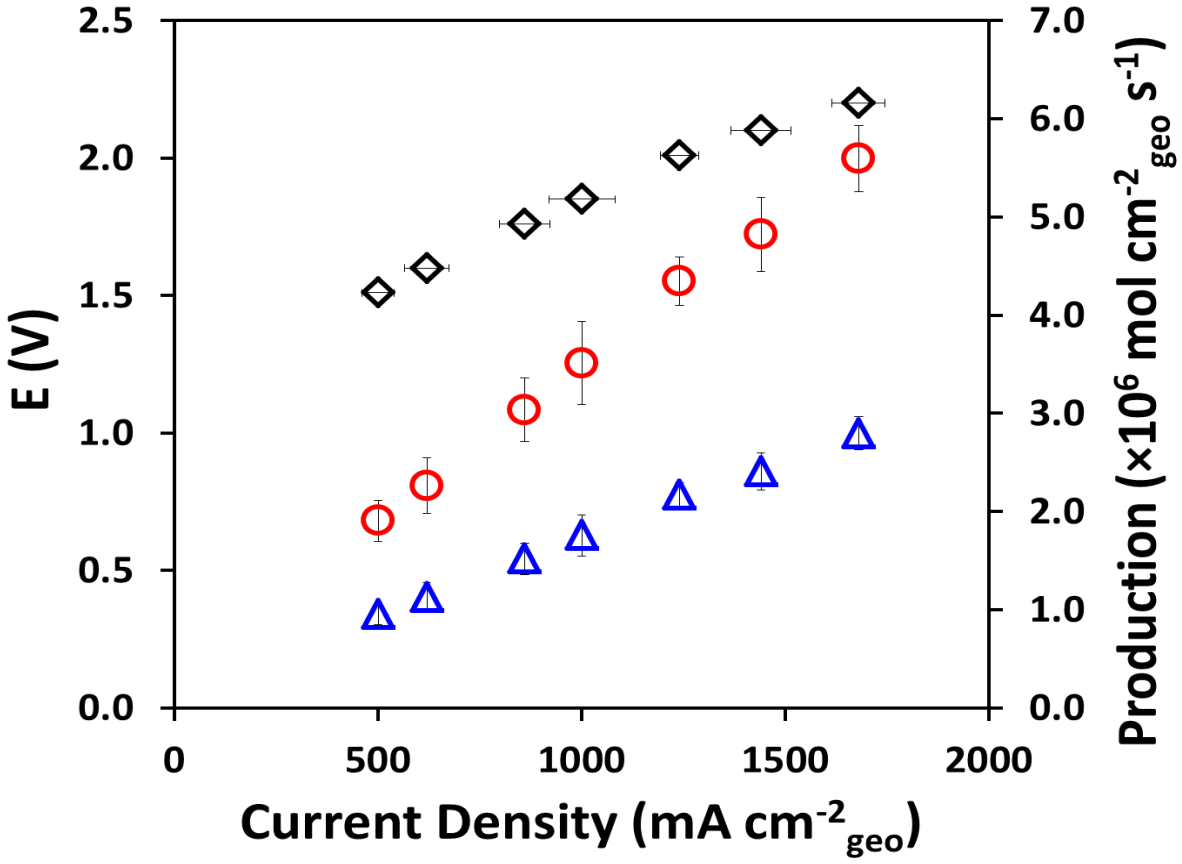

Figure S14. CO_2-purged SMRB electrolyzer polarization curve with O_2 (blue triangle) and H_2 (red circle) production at 21 ºC.

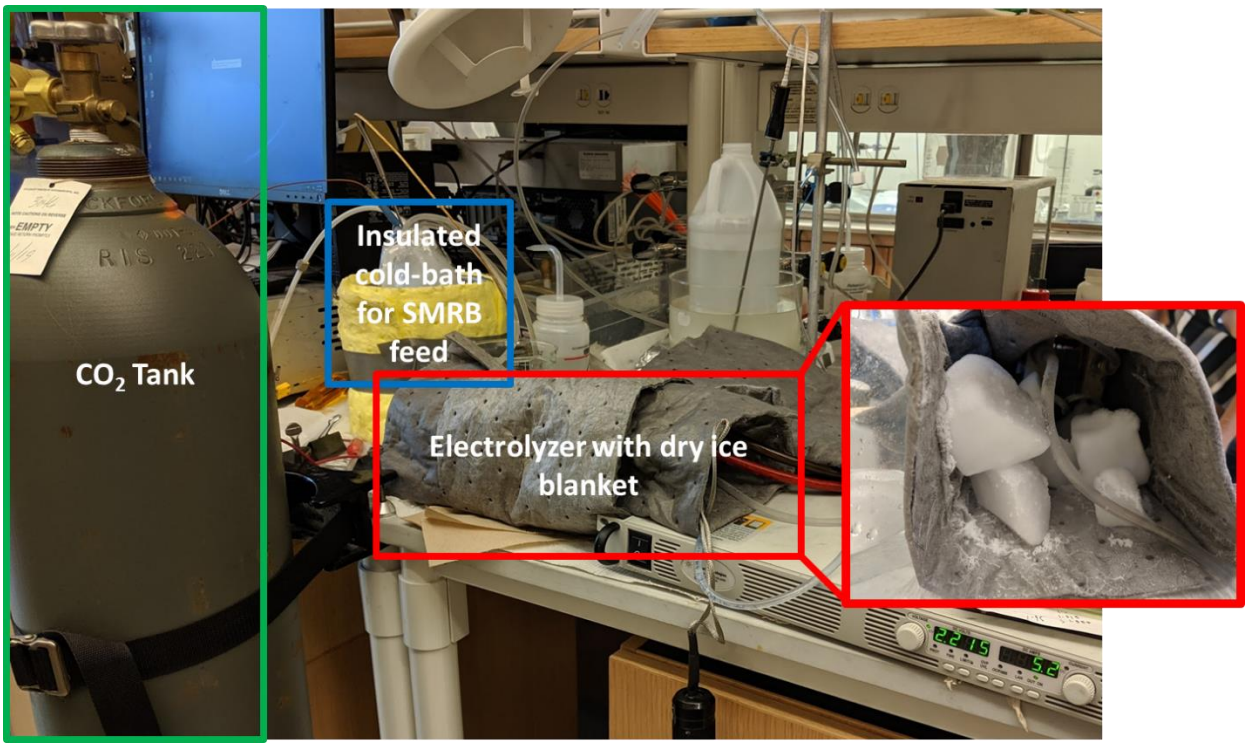

Figure S15. Electrolyzer in-lab experimental setup.

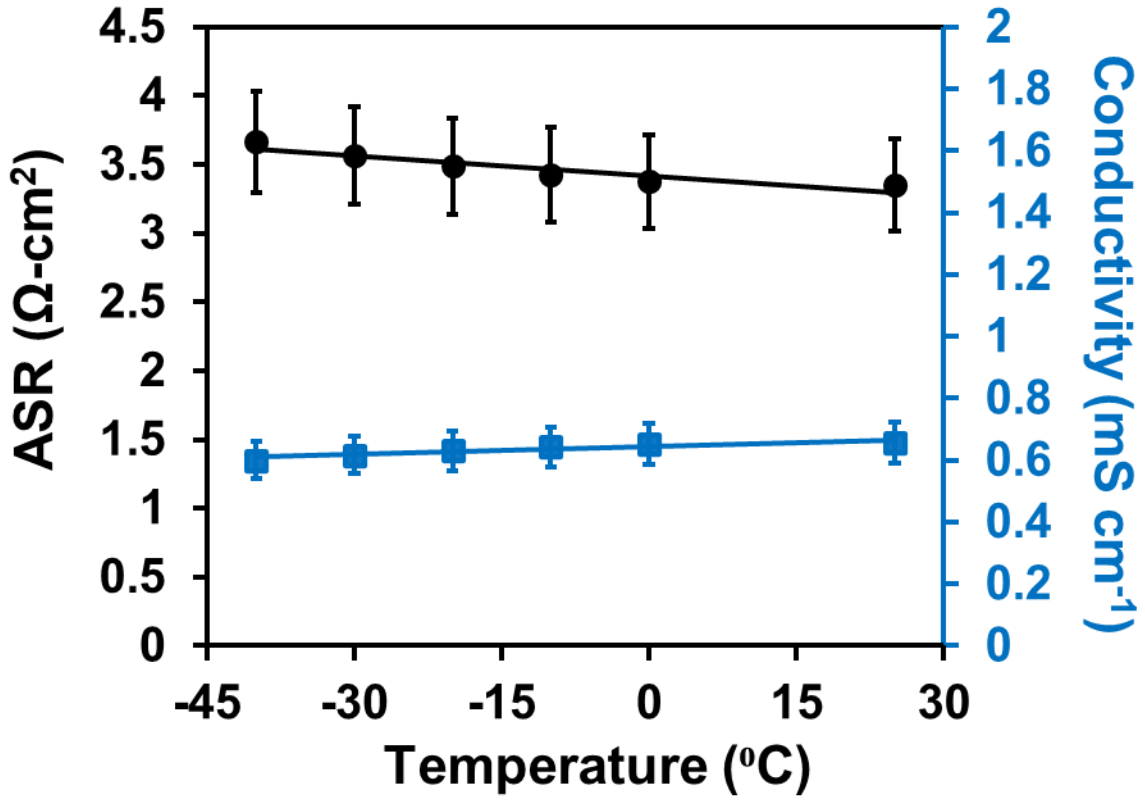

Figure S16. *In-situ* membrane area specific resistance (ASR) and corresponding conductivity for the 22µm Fumasep FAA-3-20 separators used in the SMRB electrolyzers. The values represent perchlorate ion conductivity and are extracted from the high frequency resistance obtained from the electrochemical impedance spectra in **Figure S17**.

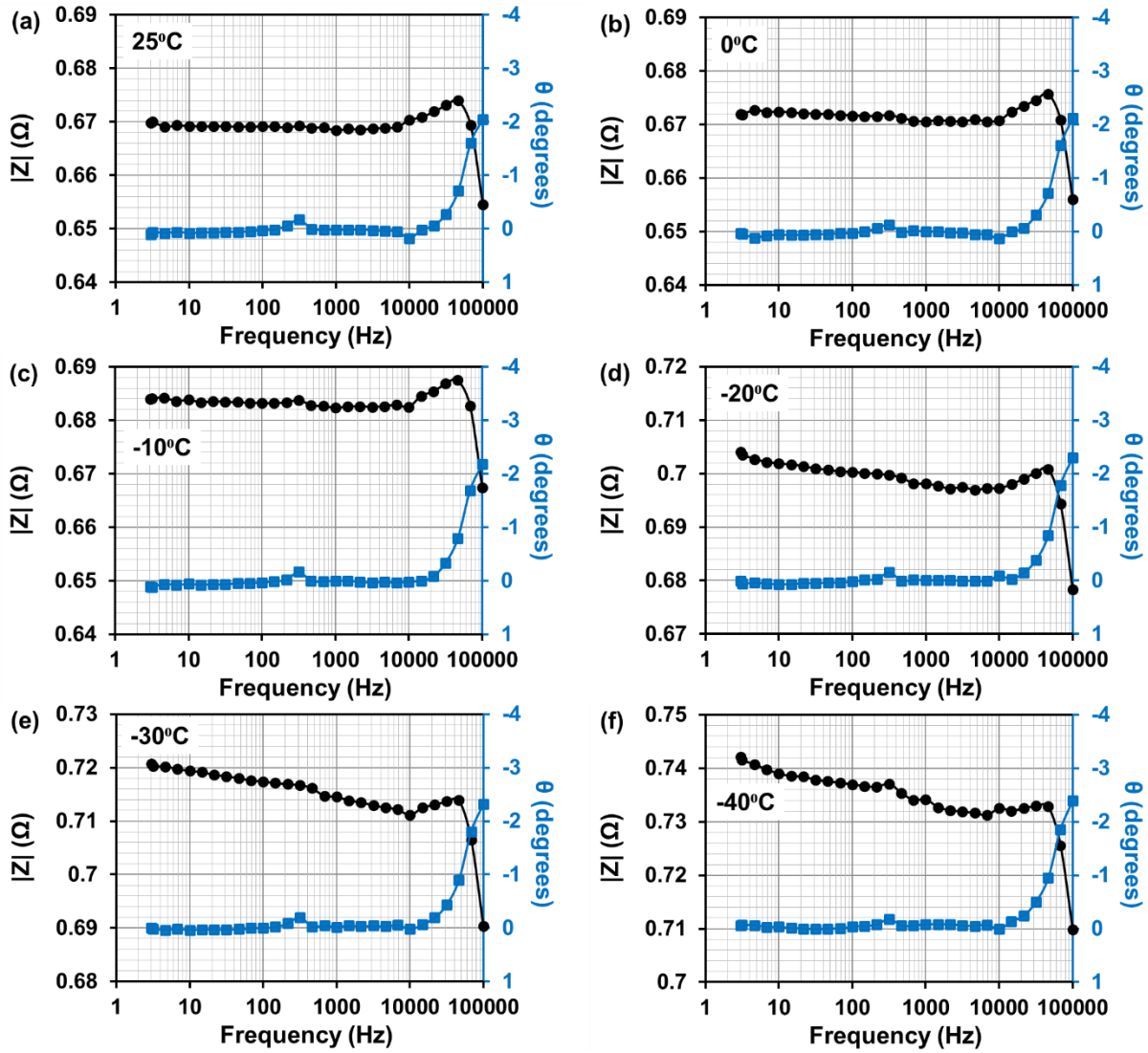

Figure S17. Bode diagrams depicting the EIS response of SMRB electrolyzers with 22µm Fumasep FAA-3-20 separators, assembled and operated as detailed in text. The resistance values obtained at 0° phase angle are used to calculate ASR and conductivity in **Figure S16**.

Table S1. Martian regolith composition as determined from surface samples by the Phoenix lander (3).

Ion	Measured concentration (moles x 10^{-5}/cm^3)
Na^+	3.23
K^+	0.74
Ca^{2+}	1.28
Mg^{2+}	7.31
Cl^-	0.97
ClO_4^-	5.83
SO_4^{2-}	13.4

Table S2. Physical and chemical properties of Fumasep FAA-3-20 AEM as listed by the manufacturer.

Property (units)	**Manufacturer listed values**
Thickness (μm)	18 - 22
Ion exchange capacity ($mmol_{Cl-}$ g^{-1})	1.65 – 1.85
Area specific resistance in Cl^- form (Ω-cm^2) measured in 0.5M NaCl at 25ºC	< 2
Conductivity in Cl^- form (mS cm^{-1})	>5
H_2O uptake at 25ºC (wt%)	7
Swelling in H_2O at 25ºC (%)	<2

Source: https://fuelcellstore.com/spec-sheets/fumasep-faa-3-20-technical-specifications.pdf